COMMUNICATION

Check for updates

Origin of discrete resistive switching in chemically heterogeneous vanadium oxide crystals†

B. Raju Naik,[a] Yadu Chandran,[a] Kakunuri Rohini,[a] Divya Verma,[a] Shriram Ramanathan[b] and Viswanath Balakrishnan ⓘ *[a]

Phase changes in oxide materials such as VO_2 offer a foundational platform for designing novel solid-state devices. Tuning the V:O stoichiometry offers a vast electronic phase space with non-trivial collective properties. Here, we report the observation of discrete threshold switching voltages (V_{th}) with constant ΔV_{th} between cycles in vanadium oxide crystals. The observed threshold fields over 10 000 cycles are $\sim 100\times$ lower than that noted for stoichiometric VO_2 and show unique discrete behaviour with constant ΔV_{th}. We correlate the observed discrete memristor behaviour with the valence change mechanism and fluctuations in the chemical composition of spatially distributed VO_2–V_nO_{2n-1} complex oxide phases that can synergistically co-operate with the insulator–metal transition resulting in sharp current jumps. The design of chemical heterogeneity in oxide crystals, therefore, offers an intriguing path to realizing low-energy neuromorphic devices.

New concepts

This study investigates insulator–metal transition (IMT) materials in the V:O system for neuromorphic applications. Unlike prior focus on phase pure compounds, this work explores chemically heterogeneous vanadium oxide crystals. It unveils discrete threshold switching voltages (V_{th}) with constant ΔV_{th} in both in-plane and out-of-plane test structures. The observed fields are $\sim 100\times$ lower than for stoichiometric VO_2, showcasing unique behavior over 10 000 cycles. This behavior can be correlated with valence change mechanisms and chemical composition fluctuations in spatially distributed VO_2–V_nO_{2n-1} phases. The cyclic bipolar switching stability test reinforces discrete threshold voltages, confirming valence change mechanism-based memristor performance. Variations in Magnéli phases during voltage cycling guide switching events with equal ΔV_{th}. Chemical heterogeneity and valence state fluctuations in the vanadium oxide system suggest an interesting platform for threshold switching memristor devices.

Introduction

Insulator–metal transition (IMT) materials such as VO_2 show abrupt changes in electrical conductivity under electrical or thermal stimulus and are of interest as building blocks for artificial neurons.[1–3] Intermediate metastable states might further be of interest for synaptic plasticity.[4–7] Most research on electrical switching characteristics has focused on phase pure compounds of varying strain, dimensionality, W, Al, or oxygen vacancy-doped vanadium dioxide.[8–11] Compositional heterogeneity within a single device channel to optimize the switching voltages represents an early research stage and could lead to reduced threshold switching energies compared to pristine single crystal bulk compounds. It is known that hetero-phase boundaries play a critical role in creating residual

filaments that can help guide conductive filament nucleation.[12–16] Crystalline VO_2 is a potential candidate for engineering phase boundaries, mainly because the system can accommodate large vacancy concentrations and host numerous Magnéli–Wadsley phases at different V:O ratios.[17–20] From a material's design perspective, understanding switching mechanisms and electrical properties in heterophase mixtures is essential in optimizing devices. While non-stoichiometry might often be considered a detriment to device function, it is being increasingly examined as a feature in emerging devices, and our results provide a path for reduced switching energies and discrete switching that could be of interest in stochastic circuits.

This article demonstrates a threshold-switching device with discrete V_{th} voltages in chemically heterogeneous vanadium oxide samples of in-plane and out-of-plane device geometries. Discrete switching at ultra-low voltages in non-stoichiometric vanadium oxide with spatial distribution of the VO_2 and V_nO_{2n-1} heterophase is caused by electrically driven compositional fluctuations. Switching tests conducted over 10 000 I–V cycles show reduced discrete switching points, and eventually, the discrete V_{th} voltages are stabilized to a single point. The discrete stochastic switching mechanism was explained by

[a] School of Mechanical and Materials Engineering, Indian Institute of Technology, Mandi, Himachal Pradesh, 175075, India. E-mail: viswa@iitmandi.ac.in

[b] Department of Electrical and Computer Engineering, Rutgers State University, New Jersey, Piscataway, NJ 08854, USA

population dynamics of electrochemical species and fluctuations in their valence states under applied electric field stress. This implies that during continuous electric bias switching cycles, the vanadium oxide crystal experiences compositional changes dynamically. Microstructural design of heterogeneity in the V:O system is a promising direction to explore for threshold switching devices with stochastic threshold voltages that are discretized over a large number of cycles. The investigated aspects are also relevant for the fabrication of stoichiometric VO_2 thin film devices to enable stable threshold switching over a large number of cycles under optimal unipolar electric fields.

Results and discussion

Fig. 1a illustrates the graphical representation of two terminal planar devices on a crystalline VO_2 fabricated with an approximate channel length of 40 μm and thickness of 600 nm (Fig. S1a and b, ESI†). The vapor phase-grown vanadium oxide crystal exhibits distinct dark and bright patterns with random orientations. These contrasting regions are labelled as VO_2 (vanadium dioxide) and V_nO_{2n-1} (Magnéli phase vanadium oxide), which signifies the chemical heterogeneity within the crystal. This in-plane device structure has titanium/gold (Ti/Au) as contact electrodes. For electrical characterization, tungsten tips with a tip radius of $\sim$7 μm were placed on the Ti/Au electrodes, and voltage was applied across the electrodes while the current passing through the crystal was limited by a set compliance value (I_{cc} = 10 mA). Fig. 1b shows representative current *versus* voltage (I–V) characteristics in linear and semi-log plots (inset). The V_{th} voltages are defined as the specific voltages at which vanadium oxide exhibits a transition in its resistance states, transitioning from a high resistance insulating state to a

low-resistance metallic state. Interestingly, multiple current jumps are observed at V_{th}, while no considerable variations are seen during the transition from the low resistance to high resistance state. It is known that oxygen deficiencies highly influence the structural stability and IMTs and in turn can reduce the threshold fields significantly. The planar device exhibits a large number of discrete threshold switching points (nearly $\sim$9) within the first 100 I–V cycles, with a consistent voltage difference (ΔV_{th}) between cycles, which is an intriguing behaviour in VO_2. The marked numbers indicate the direction of the current flow in Fig. 1b. For precise identification of discrete threshold voltages, all I–V plots are shown in a linear scale, with a semi-log plot as the inset for visualization. The scatter plot in Fig. 1c illustrates the V_{th} voltages as a function of the number of cycles, revealing a ΔV_{th} of 0.74 V. In this study, it is observed that, during the first 100 I–V repetitive cycles, the voltage required to transition the device from high resistance to low resistance is significantly smaller compared to stoichiometric VO_2. Also, the magnitude of the resistance change in the insulator to metal is approximately 10^3, which is one order less than stoichiometric VO_2. To further verify this intriguing behavior, we performed device-to-device variation tests. It was observed that for a device with an almost identical channel length, the number of V_{th} points and voltage required for switching are different. However, the ΔV_{th} remains constant for each device (D-1 to D-4), as shown in Fig. S2a–d, ESI.† The statistical analysis given in the tables beneath Fig. S2 (ESI†) clearly indicates that all four devices have different standard deviations (1.12, 1.28, 0.13, and 0.25 V), and their actual ΔV_{th} are different. This analysis effectively highlights the variability among the devices, as reflected in their standard deviations and actual threshold voltage differences (ΔV_{th}). We performed material characterizations to investigate the origin of the observed discreteness in voltages. Fig. 1d shows an optical microscopy image of VO_2 crystals with clear surface contrast in terms of dark and bright regions. We have used yellow and red arrows to illustrate the bright and dark regions within a VO_2 crystal. The FESEM image in backscattering mode (Fig. 1d, inset) confirms the presence of compositional variations in the VO_2 crystals. Furthermore, X-ray photoelectron spectroscopy (XPS) analysis of the elemental composition revealed that the sample surface comprises 67.6 at% in the +4 oxidation state and 32.3 at% in the +5 oxidation state, indicating a mixed-phase composition, as illustrated in Fig. 1(e). The X-ray diffraction (XRD) analysis (Fig. 1f) shows that the crystals are chemically heterogeneous, as evidenced by a low-intensity impurity peak denoted by '@', which corresponds to Magnéli phase oxide (V_2O_3). Many non-stoichiometric crystalline solids show the co-existence of multiple phases. For example, phase management in the single crystalline VO_2 nanobeam has shown coexisting phases by tuning the composition.[18] In brief, we would like to highlight that the vanadium oxide crystals presented here are chemically heterogeneous involving coexisting phases. Detailed structural investigations were carried out by Raman spectroscopy within bright and dark regions (Fig. S3a and b, ESI†). It has been reported that the lower frequency
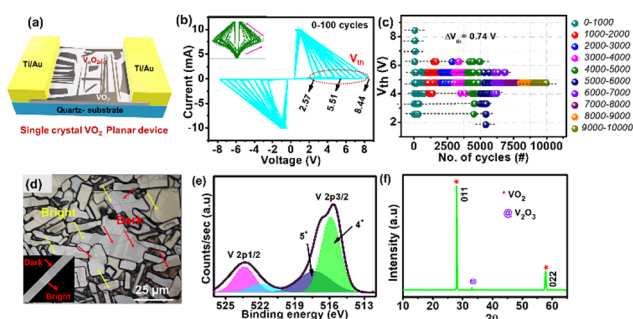

Fig. 1 A schematic of the planar vanadium oxide device current–voltage measurements and their material characterizations. (a) Schematic of the chemically heterogeneous VO_2 crystal planar device, with an approximate channel length of 40 μm. (b) I–V characteristics showing multiple transition points in the linear graph and the inset shows the semi-log plot. (c) Threshold switching scatter plot representing several I–V cycles *vs.* V_{th}, having ΔV_{th} of 0.74 V. (d) Optical microscopy image of VO_2 crystals showing chemical heterogeneity (bright and dark patterns are shown by yellow and red arrows) and the inset shows the backscattering SEM image. (e) V 2p scan from XPS analysis representing multiple oxidation states (+4 and +5). (f) XRD pattern confirming chemical heterogeneity with the presence of Magnéli phase represented with symbol '@'.

peaks correspond to V–V vibrations, while the higher frequency peaks (>300 cm^{-1}) correspond to V–O vibrations. Since the VO$_2$ crystals formed using CVD show microdomains with different optical contrasts, we performed Raman spectroscopy in both bright and dark regions. It has been observed that the V–V vibrations at 193 and 225 cm^{-1} have reversed intensity ratios at neighbouring bright and dark regions of the same VO$_2$ crystals. Also, the Raman modes of the V–O bond have shifted to lower frequencies. The reversal of the intensity ratio of the V–V dimers is attributed to the lattice strain present within the sample, affecting the out-of-plane vibrations in the cR due to the shortening of the V–O bonds.[21] Similarly, the shift in V–V and V–O vibrations to lower frequencies also relates to the oxygen deficiency in the sample.[22] Thus, comparing the Raman modes of both bright and dark regions, it can be concluded that the bright region is oxygen deficient compared to the dark region.

In addition, the heterogeneity of the crystalline VO$_2$ was verified and confirmed using various techniques, including energy dispersive spectroscopy (EDS) (Fig. S4a and b, ESI†), differential scanning calorimetry (DSC) heating and cooling curves (Fig. S5a–c, ESI†), and *in situ* electrical and mechanical testing (Fig. S6a–c, ESI†). All these analyses confirm that the as-grown crystal is not fully stoichiometric VO$_2$; instead, it is non-stoichiometric, with the majority of the volume fraction dominated by stoichiometric VO$_2$. We conducted similar experiments on polycrystalline samples to verify this unique discrete behaviour. Fig. 2a shows the schematic of the electrical measurements conducted in an out-of-plane geometry, with polycrystalline (PC) VO$_2$ sandwiched between a bottom platinum (Pt) electrode and top Ti/Au electrodes. The obtained I–V characteristics for a repetitive cyclic voltage test over 100 cycles display similar conspicuous discreteness in V_{th} voltages, as shown in Fig. 2b. Thus, the device V_{th} voltages are highly unstable and bounce back and forth with multiple I–V cycles.

Interestingly, the ΔV_{th} between cycles remains constant for the polycrystalline VO$_2$ device. The same is consistent with our observation on planar VO$_2$, mentioned earlier. The scatter plot shows a ΔV_{th} of 1.02 V over 10 000 cycles (Fig. 2c). Despite the differences in device geometries and crystallinity of the VO$_2$ devices, they exhibit the same unique discreteness in V_{th} with equal ΔV_{th} behavior during I–V cycles. The PC-VO$_2$ crystals were further verified by microscopic and spectroscopic analysis. Fig. 2d shows the SEM image and indicates the microparticle nature of the PC-VO$_2$. Fig. 2e shows the XPS analysis with multiple oxidation states +3, +4, and +5. To elucidate the compositional variation in the vanadium oxide crystal, we have performed XPS depth profiling, as shown in Fig. S7, ESI.† It is observed that the top surface contains more +5 oxidation state along with dominant +4 oxidation state while only negligible +5 oxidation state is observed after 100 nm depth. The XRD analysis shown in Fig. 2f confirms that VO$_2$ predominantly dominates the sample. Based on the electrical measurements, it is possible to claim that low-field switching and discrete switching over many cycles are dominated by ionic transport, supported by sweep polarity-dependent electrical I–V measurements. Fig. 3a shows I–V characteristics during a positive voltage sweep with multiple threshold switching points. Fig. 3b shows stabilized I–V characteristics within 900–1000 cycles, and the scatter plot in Fig. 3c shows V_{th} distribution over 1000 cycles. The off-state currents obtained in the I–V characteristics from Fig. 3a display a current of 0.296 mA before cyclic stabilization, while Fig. 3b exhibits an off-state current of 1.642 mA after stabilization. This is also true for negative polarity I–V cycles, as shown in Fig. 3d–f. This suggests that IMT is a dominant mechanism after stabilization, and valence change-based filament formation plays a dominant role before cyclic stability. This provides clear insights into the electroforming of conducting filaments with the aid of charge transfer and also reveals the effect of polarity on stochastic threshold switching during voltage sweeps. Dark and bright pattern motion dynamics further verify these compositional changes on the VO$_2$ crystal under microscopy during heating–cooling cycles (Fig. S8a–g, ESI†). These motion
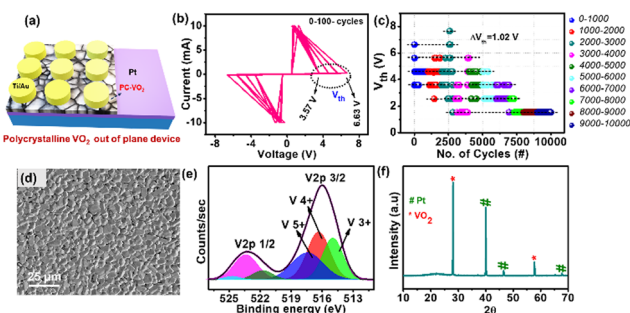

Fig. 2 Depicts the vertical device current–voltage measurements of the poly crystalline vanadium oxide and their material characterizations. (a) Schematic of the polycrystalline out of plane device, with platinum and gold as the top and bottom electrodes, respectively. (b) I–V characteristics showing multiple transition points in the linear graph and the inset showing the semi-log plot. (c) Threshold switching scatter plot representing several I–V cycles *vs.* V_{th}, ΔV_{th} of 1.02 V. (d) SEM image of polycrystalline vanadium oxide showing grain-like structures. (e) V 2p scan from XPS analysis representing multiple oxidation states (+3, +4 and +5). (f) XRD pattern confirming the VO$_2$.
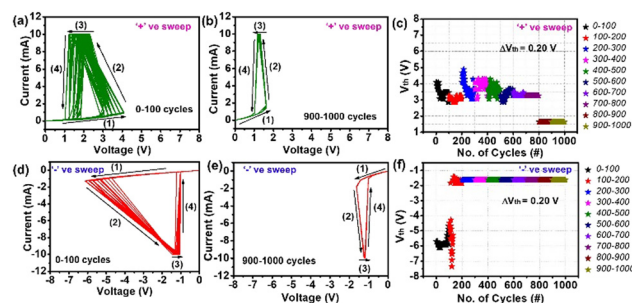

Fig. 3 Sweep bias polarity dependent electrical transport measurements of the vanadium oxide crystalline sample. (a) Discrete threshold switching over the initial 0–100 I–V cycles during positive sweep. (b) Switching between 900–1000 cycles. (c) Distribution of V_{th} voltages *vs.* number of cycles with ΔV_{th} of 0.20 V. (d) Discrete switching in negative sweep for the initial 0–100 cycles. (e) Switching between 900–1000 cycles. (f) Distribution of V_{th} voltages *vs.* number of cycles with ΔV_{th} of 0.20 V.

dynamics are observed near room temperature and differ from the typical contrast variations from insulator–metal transition near 68 °C in the VO$_2$ crystals (Fig. S9a–c, ESI†).

In earlier works, a systematic reduction in threshold voltage has been demonstrated by introducing oxygen vacancies in VO$_2$ by controlled annealing.[23] Oxygen vacancies have been extensively studied for their effect on electrical transport in VO$_2$. For instance, excess oxygen vacancies increase the carrier concentration and promote metallicity, suppressing abrupt phase transition in VO$_2$.[24] Electrochemical creation and annihilation of oxygen vacancies at the nanoscale by applying an electric field through the AFM tip on VO$_2$ is known to affect the transport properties.[25] The approach of engineering the stoichiometry in VO$_2$ by introducing either oxygen vacancies or excess oxygen has been explored for stabilizing rutile or triclinic phases.[18,26] Inherent structural stochasticity with four variants of the M1 phase during insulator–metal transition in VO$_2$ has been observed *via in situ* electrical triggering in TEM. However, it is unclear how the structural stochasticity is directly related to the threshold voltages, especially when a greater number of discrete threshold voltages are observed beyond four structural variants.[27] Furthermore, the electric field triggered the formation of V$_5$O$_9$, conducting filaments in VO$_2$, also reported to contribute to non-volatile switching at low threshold voltages.[28,29] Such non-stoichiometric phases promote resistive switching at very low voltages despite large channel lengths. Earlier reports found that a stoichiometric VO$_2$ demanded significantly high threshold electric fields in the range of 10^6 to 10^7 V m^{-1}.[30] Conversely, chemically heterogeneous VO$_2$ shows a remarkable reduction of electric fields compared to stoichiometric VO$_2$. The estimated threshold electric fields for switching the device vary between 4×10^4 V m^{-1} and 21×10^4 V m^{-1} within the investigated 10 000 I–V cycles for VO$_2$ planar devices with a channel length of ~40 μm. Similarly, very low threshold electric fields, varying between 0.6×10^4 V m^{-1} and 2.6×10^4 V m^{-1}, are observed over 10 000 repeated I–V cycles in a heterogeneous polycrystalline VO$_2$ film with a thickness of 250 nm in the out-of-plane geometry. Note that the estimation of threshold electric fields is carried out with the in-plane channel length of ~40 μm, and in reality, the actual channel length might be much lower as the conducting oxygen deficient Magnéli phase is spatially distributed.

We correlate the mechanism of low V_{th} voltages that show discreteness with constant ΔV_{th} with dynamic fluctuation in composition and related shuttling of oxygen ion vacancies. Fig. 4 shows a schematic of the mechanism for discrete threshold voltages during reversible I–V sweeps. Fig. 4a and b show a representative I–V hysteresis curve with six segments of operation, and crystalline VO$_2$ with dark and bright patterns, respectively. Segment I–III is for a positive voltage sweep and IA–IIIA for a negative voltage sweep. During part I, the reduction process occurs with the creation of oxygen vacancies. As the voltage increases, a conducting filament by V$_n$O$_{2n-1}$ starts forming by migration of oxygen vacancies across VO$_2$, as shown in Fig. 4c. The V$_n$O$_{2n-1}$ (bright region) filament formation is due to small volume fractions of Magnéli phases between VO$_2$
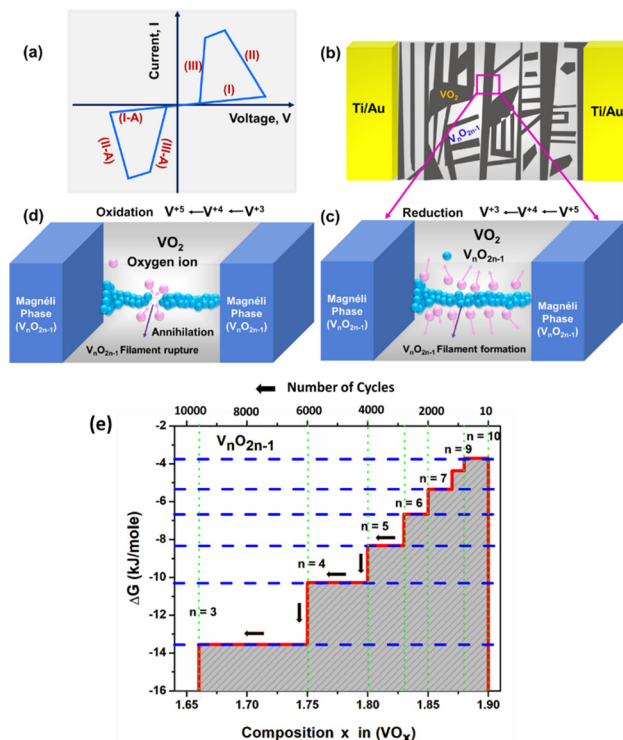

Fig. 4 Schematic illustration of the conduction mechanism of chemically heterogeneous vanadium oxide with the help of oxygen vacancies and ionic movement. (a) Schematic of I–V hysteresis. (b) Schematic representation of the chemically heterogeneous vanadium oxide device with bright and dark patterns. (c) I and I-A represent the vacancy-induced filament formation across Magnéli phases, and II and II-A represent the phase change of VO$_2$. (d) III and III-A represent the filament rupturing due to vacancy annihilation. (e) Discrete free energy changes against compositional evolution are observed during electrical switching cycles. The discrete free energy changes with respect to the composition are estimated for redox reactions involving charge transfer, while the mentioned number of cycles in the figure is approximate to indicate the free energy variations over repeated cycles.

(dark region) as shown in Fig. 4b marked region. This filament formation increases the current rapidly, and Joule heating becomes significant to drive the subsequent growth of the conducting filament.[31] These filaments act like a guiding path and their formations are sensitive to these dynamic fluctuations in oxygen ion vacancy concentration. In segment II, the insulator–metal transition is triggered once the required threshold voltage is reached, leading to an abrupt increase in current. During segment III, oxidation occurs, and these filaments start rupturing by annihilation of oxygen vacancies by migration of oxygen ions, which results in an abrupt decrease in current (Fig. 4d). The above processes are also valid in the negative voltage direction. Since the reduction process and filament formation require more supply of oxygen vacancies over repeated electric cycles, the filament formation path becomes random, generating several V_{th}. On the contrary, for rupturing, even a minute annihilation of oxygen vacancies can break the conducting filament. During repeated electrical cycles, the conducting filament thickness increases, which results in a decrease in V_{th}, which is evident from the results of both planar and out of plane VO$_2$ samples.

Nevertheless, the origin of discreteness in V_{th} with an equal voltage difference between each consecutive current–voltage characteristic of VO$_2$ needs further validation. It is possible to correlate the electrochemical redox reaction during the electrical triggering and changes in threshold voltage. We use the Nernst equation to understand the mechanism described below.[32]

$$E = E^{\circ} - \frac{2.303RT}{zF}\log(K) \qquad (1)$$

where E = formal potential, E° = standard potential, K = reaction quotient, z = number of charge transfer, F = Faraday's constant (96 500 C mol^{-1}), R = gas constant (8.314 J mol^{-1} K^{-1}) and T = temperature (298 K). To make the above expression relevant for gas phase reactions, the reaction quotient has to be expressed in partial pressures of reaction species instead of their ionic concentrations. For all reactions involving the formation of the Magnéli phase (V$_n$O$_{2n-1}$) in VO$_2$, the expression can be simplified as shown below.

$$E = E^{\circ} - \frac{2.303RT}{zF}\left[\frac{1}{2}P(\mathrm{O}_2)\right] \qquad (2)$$

Assuming the constant E° value of 0.34 V for all reactions involving reduction of V^{+4} to V^{+3} with fractional charge transfer, formation of V$_2$O$_3$, V$_3$O$_5$, V$_4$O$_7$, V$_5$O$_9$, *etc.*, values of E, and free energy changes ($\Delta G = -nFE$) are calculated and shown in Table S1 (ESI†). It is possible to evolve several phases derived from a parent structure by crystallographic shear (c.s.). Such systematic composition variations have been demonstrated in TiO$_2$ by incorporating c.s structures. For example, Magnéli phases of Ti$_n$O$_{2n-1}$ wherein n is varied from 4 to 9, resulting in derived structures from TiO$_2$, a rutile type with regular crystallographic shear on the (121) planes.[33] Moreover, it is known that slight changes in composition can be accommodated by varying only the orientation without any changes in the number of c.s. planes. When the VO$_2$ undergoes slight reduction, the oxygen deficiency may be accommodated by disordered c.s. planes. As the oxygen deficiency increases, they form parallel ordered groups, forming lamellae structures.[33] In the present case, we have observed lamellae-like structures with parallel microdomains of various sizes that are seen in optical and electron microscope images. TEM bright field images and selected area diffraction patterns with superlattice reflections of such micro domain structures in the VO$_2$ crystals are shown in Fig. S10, ESI† in agreement with earlier work on Ti$_n$O$_{2n-1}$.[34] The revealed lamellar and micro domain structures in the TEM bright field images, Fig. S10(a) and (b) (ESI†) along with the superlattice reflections in the electron diffraction patterns provide clear evidence for the oxygen deficient heterogeneous structure of vanadium oxide. Interestingly such heterogeneity can be achieved in both oxygen deficient and oxygenated VO$_2$ with excess oxygen. During the reduction and oxidation, creation of excess cations and/or oxygen may flow up or flow down the c.s. planes, respectively, during voltage sweeps instead of limited only to thermal processing at high temperatures. Note that such minute compositional variations, introduced by annealing at high temperatures with controlled partial pressure of oxygen, are known to induce discretized free energy changes in Ti$_n$O$_{2n-1}$.[33] In the present case, theoretical calculation shows a similar feature of discrete free energy changes against their compositions with different n values for V$_n$O$_{2n-1}$, as shown in Fig. 4e. It is known that the stability range of each of these Magnéli phases will be small in the order of a few kJ moles^{-1}. Since the variations in the compositions are minimal, the step heights are also very similar, 0.65 kJ mole^{-1} when n varies from 9 to 11. At the same time, for lower values of n, the composition variations and the related step heights are large, evident from Fig. 4e. The presented free energy change against the composition for varied ratios of O/V is calculated with the fractional charge transfer, while the mentioned number of cycles is roughly approximated to correlate with the experimental observation of cycle-dependent V_{th}.

Variation in the composition and valence state during repeated cycling influences the value of E and results in discrete free energy changes for forming several non-stoichiometric phases. Because the memristive switching effect in the transition metal oxide memories is often associated with the electrochemical valence change mechanism under electrical triggering, the threshold voltage, VT, and E are correlated.[35] The electrochemical valence state fluctuations may occur during the repeated electrical switching in VO$_2$ in the solid state. Such dynamic electrochemical changes have been reported in the literature for transition metal oxide-based memristors.[36,37] The observed discreteness in the V_{th} voltages that are seemingly random in their occurrence over 10 000 repeated cycles could be explained by the variation in species undergoing valence change and the formation of several non-stoichiometric Magnéli phases during positive and negative voltage sweeps. In this scenario, the actual triggering voltage will be a random variable $R(VT)$, which may change due to the valence state reaction's highly repeated threshold voltage, V_x and formal potential (E). Note that any slight variation in the population dynamics of electrochemical species and their valence states between the positive and negative voltage sweeps would affect the V_T as per the following expression with definite voltage difference (ΔV_{th}) across multiple switching events.

$$R(VT) = V_x \pm n\Delta V_{th} \qquad (3)$$

Here, the n is an integer (n = 1, 2, 3, 4, *etc.*) related to the compositional variations in Magnéli phase (V$_n$O$_{2n-1}$) that forms the conducting channel during the switching cycles. The population dynamics of V^{+4} species undergoing valence state are stochastic but result in switching at discrete threshold voltages dictated by the driving force for electroforming of Magnéli phase channels. Furthermore, the ΔV_{th} is related to the step heights in the free energy change plot (Fig. 4e). The discreteness in threshold voltages with constant ΔV_{th} arises due to the dynamic changes in composition of the Magnéli phase, wherein 'n' takes larger values above 5. In other words, the mechanism of resistive switching at the threshold voltage is governed by IMT and valence change-induced ionic species

transport in VO$_2$; the discrete variation in threshold voltages is arising due to fluctuations in composition, induced by electrical cycling. To understand the individual contributions of IMT and valence change in restive switching we carried out temperature dependent electrical measurements across the IMT. Transport measurement was performed at elevated temperatures, and with increasing temperature, the E_{th} values decrease, and beyond 68 °C, VO$_2$ transitions into a metallic state, as shown in Fig. S11a and b, ESI.† We performed temperature-dependent I–V characteristics measurements over 100 cycles at temperatures approximately 7–8 °C below and above the VO$_2$ phase transition temperature. These results suggest that the discrete resistive switching behaviour over repeated cycles in the temperature range of 25–60 °C is dominated by the valence change mechanism. The electrical transport behaviour at $\sim$70 °C is dominated by IMT behavior characterized by linear I–V curves (Fig. S12, ESI†). Nevertheless, the actual resistive switching in chemically heterogeneous vanadium oxide may involve both valency changes as well as phase change contributions.

Due to the presence of chemical heterogeneity in the crystals, the apparent channel length between nominally insulating regions is reduced in spite of the large electrode gap in the fabricated device. Furthermore, during cycling, the V/O ratio changes with the help of c.s structures, and certain Magnéli phases are being stabilized. The variation in compositional changes and associated free energy changes of the Magnéli phases at specific O/V ratios during voltage cycling guide the switching events with equal ΔV_{th}. It is difficult to capture the compositional fluctuations happening in real-time during electrical measurements. Nevertheless, we have carried out post annealing measurements in an Ar + H$_2$ reducing environment to establish correlation between the compositional fluctuation and discrete threshold voltages. For post growth annealing treatment, Ar + H$_2$ gas was used and the annealing temperature was maintained at 850 °C. The XPS and electrical measurements of the annealed samples are shown in Fig. S13a–f and S14a–f, ESI.† In the annealed samples, the +3 oxidation state appears along with +4 and +5 oxidation states and its atomic percentage increases steadily from 24.5% to 35.2% with increasing annealing time from 15 minutes to 60 minutes. From XPS analysis, it is inferred that with increasing annealing time, there is an increase in the +3 oxidation state, indicating the formation of the oxygen-deficient phase of vanadium oxide. In addition, the I–V plots show stochastic switching in both as-grown and all annealed samples with discrete stochastic switching, as shown in S14b–f, ESI.† The current–voltage characteristics of the annealed samples result in a reduced number of transition points (V_{th}) compared to the multiple discrete V_{th} observed in the as-grown samples. The number of discrete electrical switching points is quite high in as-grown and post-annealed samples for a short duration, and those switching points decrease as the annealing time increases. This suggests that reducing multiple discrete stochastic switching points in annealed samples could be due to increased compositional variations. From the XPS and electrical measurements,

chemical heterogeneity and the observed fluctuations in valence states result in the distribution of discrete V_{th} voltages.

Conclusion

Vanadium oxide devices exhibit discrete switching behaviour driven by local fluctuations in composition. A cyclic bipolar switching stability test over 10 000 cycles shows discrete threshold voltages for several thousand cycles while early stabilization of discrete switching is observed during unipolar switching and confirms the valence change mechanism-based memristor performance. The variation in compositional changes and associated free energy changes of Magnéli phases at specific O/V ratios during voltage cycling guides the switching events with equal ΔV_{th}. The chemical heterogeneity and the observed fluctuations in fractional valence states resulted in the distribution of discrete V_{th} voltages. The demonstrated aspects may provide a novel platform for the practical threshold switching memristor device applications by exploiting the discrete pattern in the switching processes synergistically involving valence change and phase transition.

Materials and methods

The VO$_2$ crystals were grown by CVD using V$_2$O$_5$ powder precursor at 900 °C in 8 sccm of Ar gas for 2 h. Before introducing the powder precursor in the quartz tube, it was cleaned with Ar purging for 1 h at 100 sccm of flow rate. The powder precursor was kept inside a quartz boat and placed over a quartz boat on a high-temperature brick. The quartz substrate was kept 5 mm away from the powder precursor, and the temperature of the furnace was ramped from 25 °C to 900 °C with a ramp rate of 20 °C min^{-1}. The entire growth was carried out in a low-pressure environment with a pressure of 4×10^{-4} mbar. For a polycrystalline-VO$_2$, 100 nm platinum (Pt) was deposited on a quartz substrate by DC magnetron sputtering, and the same growth conditions of VO$_2$ were used with a quartz/Pt substrate.

Device fabrication

The two terminal planar device geometry on VO$_2$ crystals was fabricated with a commercially purchased shadow mask. The length between the two electrodes is 40 μm, and a 50 nm Au was deposited as an electrode material using DC magnetron sputtering. For an out-of-plane device with a VO$_2$ memristor, devices were fabricated with a planar device structure. Quartz/Pt/VO$_2$/Au were used as the substrate and electrode materials, respectively. The metal Au electrodes were deposited on VO$_2$ crystals using a shadow mask by DC magnetron sputtering.

Material characterization

The VO$_2$ crystal surface morphology was characterized using a Nikon optical microscope, and thickness was measured with an atomic force microscope (AFM) by Bruker. High-resolution images, EDS analysis, and backscattering images were recorded by field emission scanning electron microscopy (FESEM) by a

Nova Nano SEM-450. Raman vibrational modes were obtained with Raman spectroscopy by a Horiba Jobin Yvon with a 532 nm laser, crystallographic information using powder X-ray diffraction (XRD) by Rigaku, and elemental analysis using X-ray photoelectron spectroscopy (XPS) by Thermoscientific. The phase transition confirmation of VO_2 was done using differential scanning calorimetry (DSC) by a NETZSCH Geratebau GmbH. The site-specific nanoindentation was performed by using a Hysitron triboindenter 950I. The VO_2 crystals grown on a quartz substrate were attached to an iron stub and placed on the magnetic stage. A minimum of 10 indents were performed on each dark and bright region. The details of phase transition confirmation and the Raman spectrum in polycrystalline VO_2 are provided in Fig. S15a–d, ESI.† The thickness of the films and crystals was measured by atomic force microscopy (AFM) by a Bruker Dimension ICON PT. The structural characterization of crystalline VO_2 is analyzed using high-resolution transmission electron microscopy (HR-TEM) with an FEI-Tecnai G2 20 S-TWIN.

Device characterization

Electrical $I–V$ measurements were carried out using a Keysight-source measure unit B2902A model at room temperature. Resistance temperature measurements were carried out by connecting a heating stage to the probe station. For all measurements, Ti/Au were used as the electrodes.

Data availability

All the data are available within the article and in the ESI.†

Author contributions

B. R. N. carried out the research, starting from the sample preparation, material and device characterization, and involved in the entire investigation and prepared the original manuscript. Y. C. performed nanoindentation, and nano-ECR measurements. K. R. carried out CVD growth experiments. D. V. recorded optical images of the thermally-induced phase transition in the VO_2 crystals. S. R. participated in the discussion and provided critical comments on developing a mechanistic understanding of the work. V. B. conceptualized and supervised the overall work and was involved in the original manuscript preparation. All authors have contributed to manuscript writing, reviewing, and editing.

Conflicts of interest

The authors declare no competing interests.

Acknowledgements

References

1 X. Zhang, W. Wang, Q. Liu, X. Zhao, J. Wei, R. Cao, Z. Yao, X. Zhu, F. Zhang, H. Lv, S. Long and M. Liu, *IEEE Electron Device Lett.*, 2018, **39**, 308–311.

2 H. Yu, A. N. M. N. Islam, S. Mondal, A. Sengupta and S. Ramanathan, *IEEE Trans. Electron Devices*, 2022, **69**, 3135–3141.

3 W. Yi, K. K. Tsang, S. K. Lam, X. Bai, J. A. Crowell and E. A. Flores, *Nat. Commun.*, 2018, **9**(1), 4661.

4 S. Deng, H. Yu, T. J. Park, A. N. M. N. Islam, S. Manna, A. Pofelski, Q. Wang, Y. Zhu, S. K. R. S. Sankaranarayanan, A. Sengupta and S. Ramanathan, *Sci. Adv.*, 2023, **9**, 1–10.

5 Y. Wang, L. Yin, W. Huang, Y. Li, S. Huang, Y. Zhu, D. Yang and X. Pi, *Adv. Intell. Syst.*, 2021, **3**, 2000099.

6 C. Li, X. Zhang, P. Chen, K. Zhou, J. Yu, G. Wu, D. Xiang, H. Jiang, M. Wang and Q. Liu, *iScience*, 2023, **26**, 106315.

7 B. A. W. Brinkman, H. Yan, A. Maffei, I. M. Park, A. Fontanini, J. Wang and G. La Camera, *Appl. Phys. Rev.*, 2022, **9**, 011313.

8 S. M. Bohaichuk, M. Muñoz Rojo, G. Pitner, C. J. McClellan, F. Lian, J. Li, J. Jeong, M. G. Samant, S. S. P. Parkin, H. S. P. Wong and E. Pop, *ACS Nano*, 2019, **13**, 11070–11077.

9 M. W. Kim, W. G. Jung, H. Hyun-Cho, T. S. Bae, S. J. Chang, J. S. Jang, W. K. Hong and B. J. Kim, *Sci. Rep.*, 2015, **5**, 1–10.

10 Q. Lu, C. Sohn, G. Hu, X. Gao, M. F. Chisholm, I. Kylänpää, J. T. Krogel, P. R. C. Kent, O. Heinonen, P. Ganesh and H. N. Lee, *Sci. Rep.*, 2020, **10**, 1–7.

11 B. Hu, Y. Zhang, W. Chen, C. Xu and Z. L. Wang, *Adv. Mater.*, 2011, **23**, 3536–3541.

12 Y. Li, L. Loh, S. Li, L. Chen, B. Li, M. Bosman and K. W. Ang, *Nat. Electron.*, 2021, **4**, 348–356.

13 V. K. Sangwan, H. S. Lee, H. Bergeron, I. Balla, M. E. Beck, K. S. Chen and M. C. Hersam, *Nature*, 2018, **554**, 500–504.

14 L. Wang, W. Liao, S. L. Wong, Z. G. Yu, S. Li, Y. F. Lim, X. Feng, W. C. Tan, X. Huang, L. Chen, L. Liu, J. Chen, X. Gong, C. Zhu, X. Liu, Y. W. Zhang, D. Chi and K. W. Ang, *Adv. Funct. Mater.*, 2019, **29**(25), 1901106.

15 M. Lanza, K. Zhang, M. Porti, M. Nafra, Z. Y. Shen, L. F. Liu, J. F. Kang, D. Gilmer and G. Bersuker, *Appl. Phys. Lett.*, 2012, **100**(12), 123508.

16 C. Pan, Y. Ji, N. Xiao, F. Hui, K. Tang, Y. Guo, X. Xie, F. M. Puglisi, L. Larcher, E. Miranda, L. Jiang, Y. Shi, I. Valov, P. C. McIntyre, R. Waser and M. Lanza, *Adv. Funct. Mater.*, 2017, **27**(10), 1604811.

17 B. Walls, O. Murtagh, S. I. Bozhko, A. Ionov, A. A. Mazilkin, D. Mullarkey, A. Zhussupbekova, D. A. Shulyatev, K. Zhussupbekov, N. Andreev, N. Tabachkova and I. V. Shvets, *Materials*, 2022, **15**, 1–14.

18 R. Shi, Y. Chen, X. Cai, Q. Lian, Z. Zhang, N. Shen, A. Amini, N. Wang and C. Cheng, *Nat. Commun.*, 2021, **12**, 1–9.

19 Z. Zhang, F. Zuo, C. Wan, A. Dutta, J. Kim, J. Rensberg, R. Nawrodt, H. H. Park, T. J. Larrabee, X. Guan, Y. Zhou, S. M. Prokes, C. Ronning, V. M. Shalaev, A. Boltasseva, M. A. Kats and S. Ramanathan, *Phys. Rev. Appl.*, 2017, **7**, 1–13.

20 W. Brückner, W. Moldenhauer, H. Wich, E. Wolf, H. Oppermann, U. Gerlach and W. Reichelt, *Phys. Status Solidi*, 1975, **29**, 63–70.

21 E. Evlyukhin, S. A. Howard, H. Paik, G. J. Paez, D. J. Gosztola, C. N. Singh, D. G. Schlom, W. C. Lee and L. F. J. Piper, *Nanoscale*, 2020, **12**, 18857–18863.

22 J. C. Parker, *Phys. Rev. B: Condens. Matter Mater. Phys.*, 1990, **42**, 3164–3166.

23 J. Zhang, Z. Zhao, J. Li, H. Jin, F. Rehman, P. Chen, Y. Jiang, C. Chen, M. Cao and Y. Zhao, *ACS Appl. Mater. Interfaces*, 2017, **9**, 27135–27141.

24 A. Moatti, R. Sachan, S. Gupta and J. Narayan, *ACS Appl. Mater. Interfaces*, 2019, **11**, 3547–3554.

25 Y. Sharma, J. Balachandran, C. Sohn, J. T. Krogel, P. Ganesh, L. Collins, A. V. Ievlev, Q. Li, X. Gao, N. Balke, O. S. Ovchinnikova, S. V. Kalinin, O. Heinonen and H. N. Lee, *ACS Nano*, 2018, **12**, 7159–7166.

26 S. Zhang, I. S. Kim and L. J. Lauhon, *Nano Lett.*, 2011, **11**, 1443–1447.

27 S. Cheng, M. H. Lee, R. Tran, Y. Shi, X. Li, H. Navarro, C. Adda, Q. Meng, L. Q. Chen, R. C. Dynes, S. P. Ong, I. K. Schuller and Y. Zhu, *Proc. Natl. Acad. Sci. U. S. A.*, 2021, **118**(37), e2105895118.

28 S. Cheng, M. H. Lee, X. Li, L. Fratino, F. Tesler, M. G. Han, J. del Valle, R. C. Dynes, M. J. Rozenberg, I. K. Schuller and Y. Zhu, *Proc. Natl. Acad. Sci. U. S. A.*, 2021, **118**(9), e2013676118.

29 J. Jeong, N. Aetukuri, T. Graf, T. D. Schladt, M. G. Samant and S. S. P. Parkin, *Sci. 80*, 2013, **339**, 1402–1405.

30 C. Mouli, Y. Zhou, X. Chen, C. Ko, Y. Zheng and S. Ramanathan, *IEEE Electron Device Lett.*, 2013, **34**, 220–222.

31 J. Valle, N. M. Vargas, R. Rocco, P. Salev, Y. Kalcheim, P. N. Lapa, C. Adda, M. Lee, P. Y. Wang, L. Fratino, M. J. Rozenberg and I. K. Schuller, *Sci. 80*, 2021, **911**, 907–911.

32 M. Ciobanu, J. P. Wilburn, M. L. Krim, D. E. Cliffel and C. I. N. Electrochemistry, *Fundamentals of Electrochemistry*, Elsevier, 2007.

33 D. K. P. R. R. Merritt, B. G. Hyde and L. A. Bursill, *Philos. Trans. R. Soc., A*, 1973, **274**, 627–661.

34 L. A. Bursill and B. G. Hyde, *Prog. Solid State Chem.*, 1972, **7**, 177–253.

35 E. W. Lim and R. Ismail, *Electron.*, 2015, **4**, 586–613.

36 Y. Wang, K. M. Kang, M. Kim, H. S. Lee, R. Waser, D. Wouters, R. Dittmann, J. J. Yang and H. H. Park, *Mater. Today*, 2019, **28**, 63–80.

37 Y. Zhou and S. Ramanathan, *Proc. IEEE*, 2015, **103**, 1289–1310.